PHYSICS OF FLUIDS **19**, 123302 (2007)

A reduced-order model of diffusive effects on the dynamics of bubbles

A. T. Preston, T. Colonius, and C. E. Brennen
Division of Engineering and Applied Science, California Institute of Technology, Pasadena, California 91125, USA

(Received 29 March 2007; accepted 6 September 2007; published online 19 December 2007)

We propose a new reduced-order model for spherical bubble dynamics that accurately captures the effects of heat and mass diffusion. The objective is to reduce the full system of partial differential equations to a set of coupled ordinary differential equations that are efficient enough to implement into complex bubbly flow computations. Comparisons to computations of the full partial differential equations and of other reduced-order models are used to validate the model and establish its range of validity. © *2007 American Institute of Physics*. [DOI: 10.1063/1.2825018]

I. INTRODUCTION

Some common assumptions (such as polytropic compression/expansion, constant vapor pressure, and effective liquid viscosity) made in modeling the heat- and mass-transfer processes involved in spherical bubble dynamics do not accurately capture those processes.[1–4] The alternative is to solve the full set of coupled radial transport equations for each bubble, but this is too computationally intensive to implement in continuum models of complex bubbly flows. Consequently, reduced-order models that accurately capture diffusive effects are needed. Previous reduced-order models that account for thermal diffusive effects are discussed in detail in the text, and the results are compared with the model proposed herein.

As a benchmark to evaluate the reduced-order models, we numerically solve the full set of partial differential equations (PDE) for a spherical gas-vapor bubble, including heat and mass transfer in both the gas and liquid phases. Additional approximations are then used to reduce the full set of PDE from six to two; one each for the temperature and vapor concentration fields in the bubble interior. This reduced set of equations is then solved numerically for a wide range of parameters. Proper orthogonal decomposition (POD) is applied to the data in order to determine suitably averaged temperature and concentration fields. These fields suggest the adoption in the reduced order models of *constant heat and mass transfer coefficients* at the bubble wall. We show that the resulting model accurately captures diffusive effects by solving the Rayleigh–Plesset equation (RPE) coupled with two ordinary differential equations (ODEs). Analyses of the model equations for the case of small-amplitude oscillations and the case of the low Peclet number limit are also presented.

II. FULL SPHERICAL BUBBLE MODEL

We begin by delineating the complete set of PDEs that include heat and mass transfer in the gas within and the liquid outside a spherical gas-vapor bubble. Several assumptions are made at the outset: (i) The liquid is incompressible; (ii) the gas-vapor mixture is a perfect gas; (iii) Fourier's law for heat conduction in liquid and gas; (iv) Fick's law of mass diffusion for the noncondensible gas in the liquid and for the interdiffusion of vapor and gas inside the bubble; (v) constant transport properties, liquid density, and surface tension; (vi) constant transport properties for the gas; (vii) thermal equilibrium at the gas-liquid interface; and (viii) Henry's law at the gas-liquid interface. We note that there are alternatives to some of these assumptions, for example the first-order correction for liquid compressibility[5] and van der Waals equation of state for the gas.[6] However, we neglect these higher-order effects, since the focus of this paper is on modeling the impact of heat and mass transfer on bubble dynamics, rather than *all* possible competing effects. Further discussion and validation of these assumptions, under a range of conditions, are available in Ref. 7.

The resulting set of equations consists of a modified Rayleigh–Plesset equation (RPE) for the motion of the liquid, and transport equations that include heat and mass diffusion in the bubble interior. These are coupled to the transfer of heat and dissolved gas in the liquid phase through the interface conditions at the bubble wall. We refer the reader to Preston[7] for a listing of these equations and their provenance. Following Hao and Prosperetti,[8] we use a Chebychev spectral collocation method with an adaptable number of modes in the gas and liquid domains to spatially discretize the full set of equations. A fourth-order Runge–Kutta scheme is used for time integration. Demonstration of spectral convergence and further details related to the numerical method are given in Ref. 7.

In order to simplify the analysis and data reduction, it is helpful to work with nondimensional variables. In the following, the bubble radius, $R=R^*/R_0^*$, pressure, $p=P/P_0$, and temperature, $T=\mathcal{T}/\mathcal{T}_0$, are nondimensionalized by their initial (equilibrium) values denoted by the subscript 0, while the concentration, $C=\rho_V/(\rho_V+\rho_A)$, is the mass fraction of vapor. Here, the subscripts L, V, and A denote, respectively, liquid, vapor, and noncondensible gas. The nondimensional time, t, is defined using the isothermal bubble natural frequency, Ω_0.

Inserting these and other (see Sec. III A) nondimensional variables into the full bubble equations yields five nondimensional parameters: Reynolds, Weber, and Euler numbers and two Peclet numbers for thermal and mass diffusivity,

TABLE I. Dimensionless parameters, equilibrium bubble radius (R_0^*), bubble natural frequency (Ω_0), and the various forcing Gaussian widths (t_w) and amplitudes (A) for all computations. For convenience of reference, an example of the dimensional equilibrium radius and bubble natural frequency are quoted for each case for an air-vapor bubble in water at 298 K and atmospheric pressure. Note that Cases I through L do not contain vapor.

Case	R_0^* (μm)	Ω_0 (kHz)	Pe_T	Pe_G	Re	We	Eu	p_{vsat}	t_w	A(range)
A	4	4795	5.27	3.17	85.9	20.4	0.374	0.0229	4.79	1.05–1.40
B	4	4795	5.27	3.17	85.9	20.4	0.374	0.0229	47.9	1.00–1.10
C	4	4795	5.27	3.17	85.9	20.4	0.374	0.0229	479	1.03–1.048
D	40	435	36.4	28.8	780	168	0.348	0.0301	4.35	1.10–1.50
E	40	435	36.4	28.8	780	168	0.348	0.0301	43.5	0.95–1.00
F	40	435	36.4	28.8	780	168	0.348	0.0301	435	0.95–0.985
G	400	43.0	349	284	7711	1641	0.344	0.0308	4.30	1.10
H	4000	4.30	3475	2841	77030	16370	0.344	0.0308	0.430	1.00
I	4	4856	4.61	⋯	87.0	20.9	0.366	⋯	40.0	1.0
J	40	442	34.8	⋯	791	172	0.338	⋯	40.0	1.0
K	10	1827	9.26	⋯	204	46.2	0.348	⋯	⋯	⋯
L	50	353	42.9	⋯	987	215	0.336	⋯	⋯	⋯

$$\mathrm{Re} = R_0^{*2}\Omega_0/\nu_L, \quad \mathrm{We} = \rho_L R_0^{*3}\Omega_0^2/S,$$

$$\mathrm{Eu} = P_0/\rho_L(R_0^*\Omega_0)^2, \quad \mathrm{Pe}_T = \rho_{\mathrm{GV}} c_p R_0^{*2}\Omega_0/K_{\mathrm{GV}}, \quad \text{and}$$

$$\mathrm{Pe}_G = R_0^{*2}\Omega_0/D,$$

where ρ_{GV}, c_p, and K_{GV} are the density, specific heat, and thermal conductivity of the gas-vapor mixture, D is the diffusivity of the initial gas-vapor mixture, and S is the surface tension (D and S are assumed constant). The nondimensional vapor saturation pressure is defined as $p_{\mathrm{vsat}} = P_{\mathrm{vsat}}/P_0$, and for the full bubble computations of this section is a function of the temperature at the bubble wall (see Ref. 7). However, in Sec. III, the bubble wall temperature is fixed and the nondimensional vapor saturation pressure is then a constant parameter. While each of the above nondimensional parameters must be specified for every computation, it is the Peclet numbers that determine the thermal and mass diffusive behavior.

We also note that internal spatially averaged, dimensionless bubble variables are denoted by an overbar and defined by

$$\bar{T} \equiv \frac{1}{V}\int_V T dV = 3\int_0^1 T(y) y^2 dy, \tag{1}$$

where r is a radial coordinate, $y = r/R$, V is the bubble volume, and T has been used as the example.

A. Cases considered and sample calculation

We subject the bubble to a prototypical Gaussian decrease of the far-field pressure,

$$p_\infty(t) = p_{\infty 0}(1 - A \exp\{-[(t - t_0)/t_w]^2\}), \tag{2}$$

where the dimensionless amplitude, A, and time scale, t_w, are varied over a range of values that mimic conditions encountered by a bubble advecting through a converging-diverging nozzle (e.g., Preston *et al.*[9]). Nondimensional parameters for all cases considered are given in Table I. To aid in the interpretation of the results, a corresponding dimensional equilibrium radius and bubble natural frequency are given for each case for air-vapor bubbles in water at 298 K.

In order to illustrate the complex diffusive processes that occur in and around the bubble, detailed results are presented for a typical case corresponding to case E with $A = 0.985$ in Table I. Figures 1(a) and 1(b) show bubble radius and pressure at the bubble center. They exhibit the typical behavior of an *inertially controlled* bubble with strong bubble collapses leading to small minimum radii and high pressures. Except for a short time near the minimum radius, the pressure

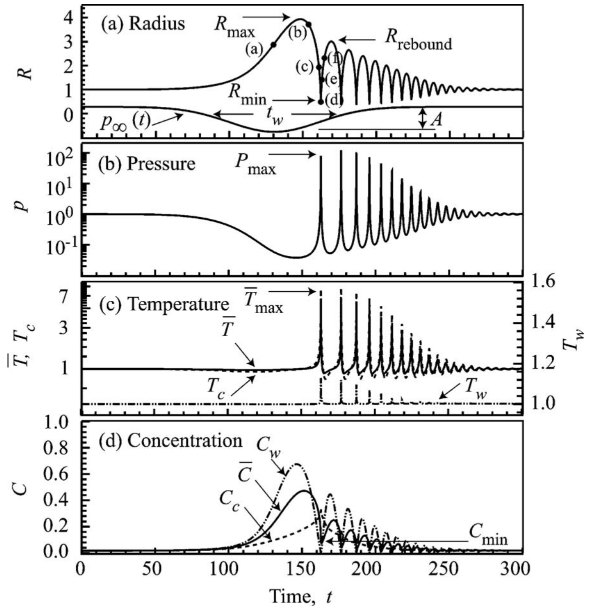

FIG. 1. (a) Bubble radius, (b) bubble pressure, (c) temperature, and (d) concentration for a 40 μm air-vapor bubble in 25°C water at atmospheric pressure (Case E, $A = 0.985$).

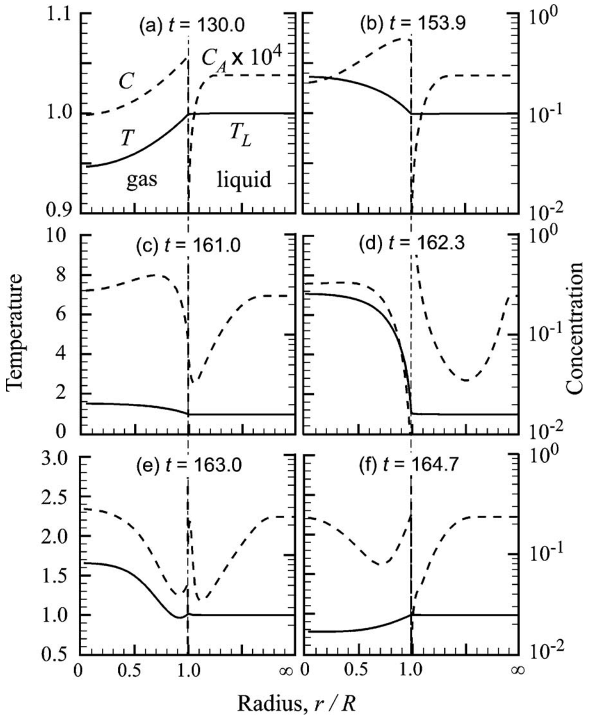

FIG. 2. Temperature and concentration profiles at different times for the computation of Fig. 1. Note that the horizontal scale changes above $r/R=1$.

throughout the bubble is nearly uniform. This result is exploited in Sec. II B.

Figures 1(c) and 1(d) plot the spatially averaged bubble temperature and vapor concentration together with their values at the bubble center (subscript c) and wall (subscript w). Changes in the bubble wall temperature are two orders of magnitude smaller than the average or center temperatures. This is a result of the liquid being *cold*, which is exploited in Sec. II B. The significant differences between the center, average, and wall values of temperature and concentration indicate substantial spatial gradients within the bubble. In particular, while C_w becomes small during collapse, $\bar{C}$ and especially C_c are well above zero indicating that slow mass diffusion is trapping vapor in the bubble on collapse.[3,10] In addition, the limiting mass diffusion during initial growth has the effect of restricting bubble growth (see Sec. IV A).

Also indicated in Fig. 1 are the maximum radius obtained during the first growth, $R_{\max}$, the second maximum radius obtained on the first rebound, R_{rebound}, the minimum radius, $R_{\min}$, maximum bubble pressure, $p_{\max}$, maximum average bubble temperature, $\bar{T}_{\max}$, and minimum average vapor concentration, $\bar{C}_{\min}$, all obtained in the first collapse. Some of these defined quantities will be used to evaluate the accuracy of reduced-order models in Sec. IV.

Figure 2 shows the temperature and concentration profiles at six times indicated in Fig. 1(a). Here the radial coordinate has been nondimensionalized by the instantaneous bubble radius, $y \equiv r/R(t)$, though the horizontal scale changes above $r/R=1$.[7] Note that the liquid temperature remains relatively undisturbed. The profiles of the gas temperature are close to quadratic in y for the slow bubble motion during initial growth in (a) and (b). During collapse, (d), there is clearly some steepening of the temperature profile near the bubble wall, which suggests a more adiabatic behavior. Shortly after collapse, (e), the profile is no longer monotonic. In fact, if we define an instantaneous heat-transfer coefficient,

$$\beta_T \equiv \frac{-\partial T/\partial y|_{y=1}}{\bar{T}-T_w}, \tag{3}$$

then β_T is negative during part of the cycle. This is more clearly illustrated in Fig. 3(a), which plots the temperature gradient at the bubble wall as a function of $(\bar{T}-T_w)$. Again the six instances in time, (a)-(f), are marked in the plot. Note that point (e) is in the first quadrant, which implies that $\beta_T<0$. In addition, part of the collapse and rebound cycle is in the third quadrant, where again β_T is negative. This counterintuitive result can be predicted by linear theory where it is caused by a phase lag between the temperature gradient and average bubble temperature (Sec. III B). It was first identified in nonlinear computations by Nigmatulin *et al.*,[11] who explained that on bubble collapse, the heat from compression is conducted to the liquid by the large thermal gradient, while during initial expansion, heat conduction is not able to compensate for the cooling of the gas wall layers caused by expansion.

The vapor concentration profiles (Fig. 2) are more complex. This is because the mass diffusion is forced by the time-varying concentration at the bubble wall, while the ther-

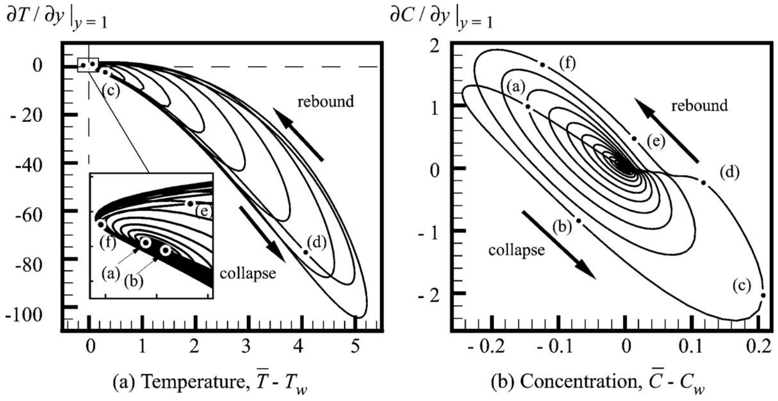

(a) Temperature, $\bar{T}-T_w$

(b) Concentration, $\bar{C}-C_w$

FIG. 3. Gradients at the bubble wall vs the difference between the average and wall values for (a) temperature and (b) concentration for a bubble in a *cold* liquid. The computation is for that of Fig. 1.

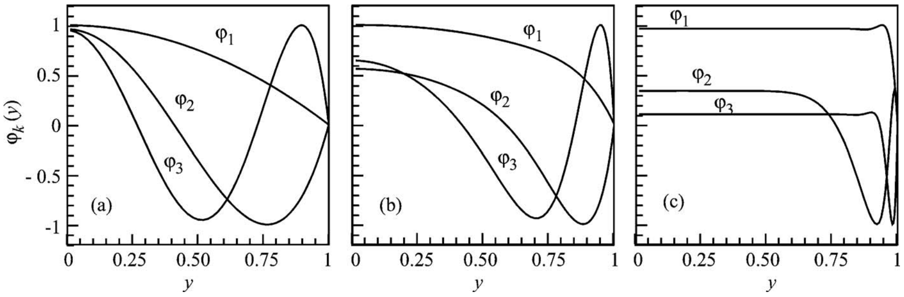

FIG. 4. First three mode shapes from the POD analysis of the temperature field for different values of Pe_T as follows: (a) $\mathrm{Pe}_T=5.27$ (Case C, $A=1.03$); (b) $\mathrm{Pe}_T=349$ (Case G, $A=1.10$); (c) $\mathrm{Pe}_T=3475$ (Case H, $A=1.00$).

mal diffusion is forced by the compression heating term acting (relatively uniformly) over the bubble interior with nearly constant wall temperature. Nonetheless, there are close parallels with the temperature profiles, particularly at instances (a), (d), and (e). Figure 3(b), which plots the concentration gradient at the bubble wall versus $\bar{C}-C_w$, indicates that at time (e) the instantaneous mass-transfer coefficient, β_C (which is defined analogously to β_T), is negative. In addition, there is considerable time spent in the third quadrant, where β_C is also negative. As with the heat transfer, this phenomenon is caused by the phase lag between the concentration gradient and the average concentration.

Referring again to Fig. 2, the mass concentration of air in the liquid, C_A, decreases near the bubble wall during the initial expansion [(a) and (b)]. This is due to the partial pressure of air in the bubble decreasing as a result of both the overall bubble expansion and the increased vapor content of the bubble. Thus air diffuses into the bubble and a layer of liquid around the bubble is depleted of air. As the bubble collapses [(c) and (d)], the concentration at the wall increases rapidly as air is forced out of the bubble. Since collapse occurs on a time scale that is fast compared to diffusion, the depletion layer remains in the liquid, but at some distance from the bubble wall. On bubble rebound [(e)], the concentration at the bubble wall begins to decrease until the situation in [(f)] is reached, where once again air is diffusing into the bubble.

B. Additional assumptions

The full computation of the preceding section illustrates some additional approximations that can be utilized to reduce the computational effort in solving the full equations, and to aid the development of reduced-order models. The following assumptions are made in the remainder of this paper: (i) The internal bubble pressure is spatially uniform,[1,11] (ii) the liquid temperature is uniform,[12] (iii) there is no diffusion of noncondensable gas in the liquid,[12] and (iv) the vapor pressure is in equilibrium at the gas-liquid interface.[12] Each of these additional assumptions has been validated for all the cases considered by comparisons with the full computations of the preceding section.[7] However, for strongly forced bubbles (e.g., large A) that have larger bubble growths and faster collapses than those considered here, the role of pressure nonuniformities and shock waves in the gas may become important.[13,14]

The set of simplified equations resulting from the above assumptions is given in Sec. III A; at this point, we note that all of the PDEs for the liquid phase, as well as the continuity and momentum equations for the gas phase, are eliminated with these approximations. The equations that remain are two PDEs for heat and mass transfer in the bubble interior, and two ODEs for the bubble radius (RPE) and the internal pressure. It is this simpler set of equations that is solved in the remainder of this paper. Finally, the reduced-order model in Sec. III A is based on these same assumptions, but with additional approximations for the heat and mass transfer that eliminate the final two PDEs in favor of a single ODE for the mass of vapor in the bubble.

C. Data set reduction

A well-known method for systematically deriving reduced-order models for PDEs is to first compute a set of orthogonal spatial modes using the proper orthogonal decomposition (POD), and then perform a Galerkin projection of the PDE onto a reduced set of the POD modes (e.g., Rowley[15] and references therein). The POD modes (or empirical eigenfunctions) are obtained from data (found, for example, by solving the full PDE as presented in Sec. II A). Simply put, given an ensemble of realizations of a field, $q(y)$ (here either the temperature or concentration field within the bubble), we find orthogonal modes, $\{\phi_k(y)\}_{k=1}^{m}$, such that the mean projection of q onto ϕ is maximized. The Galerkin projection then produces a set of ODEs describing the temporal evolution of the modal (or Fourier) coefficients. To compute the POD modes, we use the snapshot method developed by Sirovich.[16] The POD computation involves solving an m-dimensional eigenproblem for the POD modes, $\phi_j(y)$, and associated eigenvalues, λ_j. Here m is the number of equally spaced snapshots used in each POD computation, and is chosen to be large enough such that additional snapshots do not significantly impact the POD results. Each eigenvalue represents the portion of the "energy" captured by the associated POD mode. The success of the POD/Galerkin approach is not guaranteed in general, and hinges upon a large fraction of the energy being captured in a few dynamically significant modes.

The parameters that primarily determine the diffusive behavior in the bubble interior are the respective Peclet numbers for heat and mass transfer, Pe_T and Pe_G.[3] Figure 4 shows the first three POD modes for the temperature fields (concentration looks similar) for three typical computations with different values of Pe_T. For the lowest values of Pe_T, the POD modes show significant variation over the entire range of y, indicating that the diffusion penetration length is of the

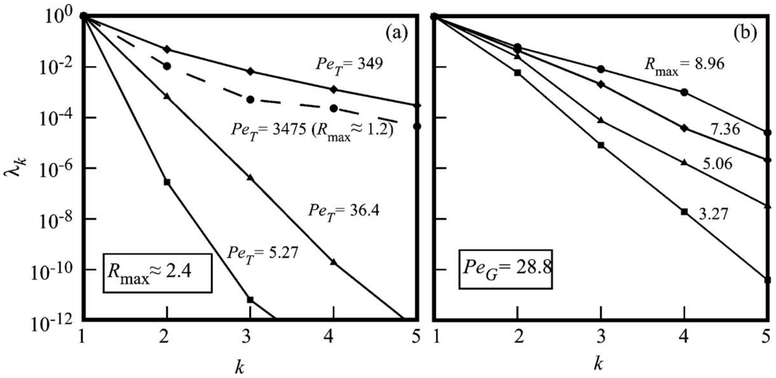

FIG. 5. First five normalized eigenvalues from the POD analysis (a) for different values of the Peclet number, Pe_T (Case C, $A=1.03$; Case E, $A=0.95$; Case G, $A=1.10$; Case H, $A=1.00$) and (b) for different values of the maximum bubble radius, $R_{\max}$ (Case F, $A=0.95$, 0.97, 0.98, and 0.985).

same order as, or greater than, the bubble radius. In particular, the first POD mode is well approximated by a quadratic in y, which corresponds to the solution of the diffusion equations in the limit of $\mathrm{Pe}_T \rightarrow 0$, as demonstrated analytically by Preston.[7] For lower values of Pe_T, the POD modes remain essentially unchanged. As Pe_T is increased, the POD modes show less variation near the bubble center. Indeed, for $\mathrm{Pe}_T=3475$, most variation occurs near the bubble wall, which indicates the diffusion penetration length is significantly smaller than the bubble radius. The manner in which the POD mode shapes depend on Pe_T is consistent with the full computations of Matsumoto and Takemura.[3] Here the POD analysis provides a convenient and concise means of summarizing such full computations.

Figure 5(a) plots the first five eigenvalues of the temperature modes for different values of Pe_T and in cases in which $R_{\max}$ is approximately constant. The eigenvalues are placed in descending order and normalized such that they sum to unity. For low $\mathrm{Pe}_T=5.27$, the decay in the eigenvalues with mode number, k, is rapid. As Pe_T is increased, this decay becomes more gradual. Similarly, Fig. 5(b) plots the first five eigenvalues of the concentration modes for computations with different $R_{\max}$ (found by changing A) and fixed Pe_G. Clearly, the rate of decay of the eigenvalues decreases as $R_{\max}$ is increased. We can conclude that modeling the diffusive behavior is likely to be more difficult for large values of Pe_T, Pe_G, and $R_{\max}$, since more degrees of freedom will be needed in the model to capture the additional energy contained in the higher modes.

Nevertheless, in all cases studied, more than 90% of the energy is contained in the first POD mode. This leads to the hypothesis that a reasonable reduced-order model can be based solely on the first POD mode. One could proceed to derive the single ODE for the modal coefficient, but this can be shown[7] to be equivalent to using a constant (average) heat/mass-transfer coefficient associated with the first POD mode,

$$\beta \equiv \frac{-\partial \phi_1/\partial y|_{y=1}}{\bar{\phi}_1 - \phi_{1w}}. \tag{4}$$

Here, ϕ_1 denotes the first POD mode, the subscript w denotes the value at the bubble wall, and the overbar is the volume average defined by Eq. (1). The heat/mass-transfer coefficient, β, forms the basis for the reduced-order model developed in the next section.

III. CONSTANT-TRANSFER COEFFICIENT MODEL

Motivated by the POD results of the preceding section, we use constant transfer coefficients to estimate the heat and mass flux at the bubble wall.

A. Modeling the fluxes: The basis for the model

We now present the model equations that employ all the assumptions mentioned in Sec. II. We begin with the RPE, which results from integrating the momentum equation for the incompressible liquid,

$$\mathrm{Eu}[p - p_\infty(t)] = R\frac{d^2R}{dt^2} + \frac{3}{2}\left(\frac{dR}{dt}\right)^2 + \frac{4}{\mathrm{Re}}\frac{1}{R}\frac{dR}{dt} + \frac{2}{\mathrm{We}R}. \tag{5}$$

Note that the equilibrium of the RPE relates the ambient pressure and the Euler and Weber numbers, $\mathrm{Eu}[1-p_{\infty 0}] = 2/\mathrm{We}$. The assumption of spatially uniform internal pressure enables the continuity and momentum equations to be integrated within the bubble interior, resulting in the following ODE for the internal bubble pressure:[1,11]

$$\frac{dp}{dt} = \frac{-3\gamma}{R}\left(p\frac{dR}{dt} - \frac{1}{\mathrm{Pe}_T}\frac{1}{R}k_w \left.\frac{\partial T}{\partial y}\right|_{y=1} - \mathcal{R}_V T_w \dot{m}_V \right). \tag{6}$$

Here $\gamma = C_w\gamma_V + (1-C_w)\gamma_A$ is the ratio of specific heats of the gas-vapor mixture, where $\gamma_V = 4/3$ and $\gamma_A = 7/5$ are the ratio of specific heats of the vapor and gas, respectively. The nondimensional thermal conductivity of the gas-vapor mixture at the bubble wall is $k_w = C_w k_V + (1-C_w)k_A$, where $k_V = K_V/K_{\mathrm{GV}}$ and $k_A = K_A/K_{\mathrm{GV}}$ are the nondimensional thermal conductivities of the vapor and gas, respectively, and K_{GV} is the thermal conductivity of the initial gas-vapor mixture. The nondimensional perfect gas constant of the vapor, $\mathcal{R}_V$, is defined shortly. The mass flux of vapor into the bubble per unit surface area is nondimensionalized by dividing by $\rho_{GV}R_0^*\Omega_0$ and then denoted by $\dot{m}_V$. It is determined from reciprocal diffusion as

$$\dot{m}_V = \frac{1}{\mathrm{Pe}_G}\frac{p}{\mathcal{R}T_w}\frac{1}{1-C_w}\frac{1}{R}\left.\frac{\partial C}{\partial y}\right|_{y=1}. \tag{7}$$

Here $\mathcal{R} = C_w\mathcal{R}_V + (1-C_w)\mathcal{R}_A$ is the nondimensional perfect gas constant of the gas-vapor mixture at the bubble wall, $\mathcal{R}_V = \mathcal{R}_V^*/\mathcal{R}_0^*$ and $\mathcal{R}_A = \mathcal{R}_A^*/\mathcal{R}_0^*$ are the nondimensional perfect gas constants of the vapor and gas respectively, and $\mathcal{R}_0^*$ is the perfect gas constant of the initial gas-vapor mixture. In the above equations, the subscript w denotes a variable evaluated at the bubble wall ($y=1$).

To close the set of equations (5)–(7), we require the concentration and temperature gradients at the bubble wall. Motivated by the POD results of Sec. II C, we model the gradients at the bubble wall using constant mass and heat-transfer coefficients, β_C and β_T, such that

$$\left.\frac{\partial C}{\partial y}\right|_{y=1} \approx -\beta_C(\bar{C}-C_w) \quad \text{and} \qquad \left.\frac{\partial T}{\partial y}\right|_{y=1} \approx -\beta_T(\bar{T}-T_w). \tag{8}$$

Note that the overbar denotes the volume average over the bubble defined by Eq. (1). For each computation, the transfer coefficients will depend on the Peclet numbers (see Fig. 4). It remains to determine the temperature and concentration at the bubble wall, and the volume averages of the temperature and concentration. Since the variation in the liquid temperature is neglected, the temperature at the bubble wall is simply the initial temperature, $T_w=T_0$, while the wall concentration is determined by assuming the vapor pressure at the bubble wall to be in equilibrium,

$$C_w = \frac{1}{1+\xi}, \tag{9}$$

$$\xi = \frac{\mathcal{R}_V}{\mathcal{R}_A}\left(\frac{p}{p_{\text{vsat}}}-1\right). \tag{10}$$

The average bubble temperature is estimated by applying the perfect gas law in a volume averaged sense to the bubble contents,

$$\frac{\bar{T}}{T_0} \approx \frac{p}{p_0}\frac{\rho_0}{\bar{\rho}} \approx \frac{p}{p_0}\frac{R^3}{R_0^3}\frac{m_{A0}+m_{V0}}{m_{A0}+m_V}, \tag{11}$$

where m_{A0} and m_{V0} are the initial masses of noncondensible gas and vapor in the bubble nondimensionalized by $\rho_{\text{GV}}R_0^{*3}$, and $R_0=p_0=T_0=1$ has been used for clarity. Results from full computations indicate that this approximation is extremely accurate. The nondimensional mass of vapor in the bubble, m_V, is determined by integrating

$$\frac{dm_V}{dt} = 4\pi R^2 \dot{m}_V, \tag{12}$$

where $\dot{m}_V$ is given by Eq. (7). The average vapor concentration is then given by

$$\bar{C} \approx \frac{m_V}{m_{A0}+m_V}. \tag{13}$$

The set of model equations (5)–(13) is now closed provided we have an estimate for the transfer coefficients. As mentioned previously, the transfer coefficients depend on the Peclet numbers and can be determined from the POD analysis. However, it is preferable for the reduced-order model not to rely on POD analysis, since, in general, one would not have access to an appropriate full computation. In the next section, we appeal to linear analysis to develop a simple method for determining the transfer coefficients as functions of Peclet numbers.

B. Linear analysis

The linearized mass and heat diffusion equations for the bubble interior can be written (see, for example, Prosperetti *et al.*[1]) as

$$\frac{\partial C'}{\partial t} = \frac{1}{\text{Pe}_G}\frac{1}{y^2}\frac{\partial}{\partial y}\left(y^2\frac{\partial C'}{\partial y}\right), \tag{14}$$

$$\frac{\partial T'}{\partial t} = \frac{1}{\text{Pe}_T}\frac{1}{y^2}\frac{\partial}{\partial y}\left(y^2\frac{\partial T'}{\partial y}\right) + \frac{\gamma-1}{\gamma}p'. \tag{15}$$

Here the primes denote small-amplitude perturbations, such that $C=C_0+C'$, $T=1+T'$, $p=1+p'$, and C_0 is the equilibrium vapor concentration. The above PDEs are supplemented by the symmetry conditions, $\frac{\partial C'}{\partial y}\big|_{y=0}=\frac{\partial T'}{\partial y}\big|_{y=0}=0$, and boundary conditions, $C'\big|_{y=1}=C_w'(t)$ and $T'\big|_{y=1}=0$. The solution to the linearized system can be written in the frequency domain as

$$\hat{C}'(y,\omega) = \hat{C}_w'(\omega)\Theta(y,\omega;\text{Pe}_G), \tag{16}$$

$$\hat{T}'(y,\omega) = \frac{\gamma-1}{\gamma}\hat{p}'(\omega)[1-\Theta(y,\omega;\text{Pe}_T)], \tag{17}$$

where the complex linear mode shape $\Theta(y,\omega;\text{Pe})$ is given by

$$\Theta(y,\omega;\text{Pe}) = \frac{\sinh\sqrt{i\omega\text{Pe}}\,y}{y\sinh\sqrt{i\omega\text{Pe}}}. \tag{18}$$

Differentiating and volume averaging Eqs. (16) and (17) yields

$$\left.\frac{\partial \hat{C}'}{\partial y}\right|_{y=1}(\omega) = -\Psi(\omega;\text{Pe}_G)\hat{\bar{C}}'(\omega), \tag{19}$$

$$\left.\frac{\partial \hat{T}'}{\partial y}\right|_{y=1}(\omega) = -\Psi(\omega;\text{Pe}_T)\hat{\bar{T}}'(\omega), \tag{20}$$

where the transfer function $\Psi(\omega;\text{Pe})$ is given explicitly as

$$\Psi(\omega;\text{Pe}) = \left\{[\sqrt{i\omega\text{Pe}}\coth\sqrt{i\omega\text{Pe}}-1]^{-1}-\frac{3}{i\omega\text{Pe}}\right\}^{-1}. \tag{21}$$

Since the transfer function depends on ω, an attempt to transform Eqs. (19) and (20) back into the time domain would result in a convolution integral, which is of little use for obtaining estimates for the transfer coefficients, and difficult to evaluate numerically.

These difficulties are overcome by approximating the transfer function in the frequency domain, such that Eqs. (19) and (20) can be inverted analytically without resulting in a convolution integral. In order to obtain real valued quantities after transforming into the time domain, we require the following property to hold for the approximation:

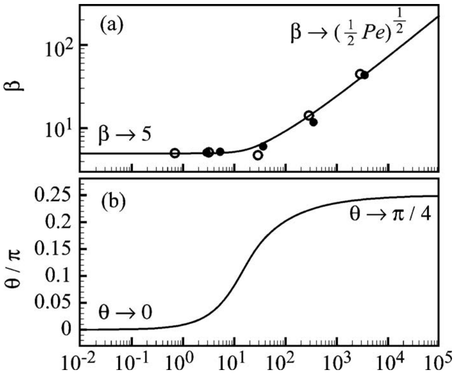

FIG. 6. (a) Real part and (b) phase of transfer function from linear analysis and β from POD analysis: (——), linear analysis; (●), POD results from temperature fields; (○), POD results from concentration fields.

$$\Psi_{\text{approx}}(\omega^*;\text{Pe}) = \Psi^*_{\text{approx}}(\omega;\text{Pe}), \tag{22}$$

where ω^* denotes the complex conjugate of ω. In the constant-transfer model, we simply use the zeroth-order term of a Taylor series expansion about some characteristic frequency, ω_0. The use of more sophisticated rational function approximations is explored in Preston,[7] but is ultimately found to give less accurate results. The characteristic frequency ω_0 that we choose is the isothermal bubble natural frequency. Within the present nondimensionalization, this corresponds to setting $\omega = \omega_0 = 1$ in Eq. (21). The appropriateness of the choice of the isothermal bubble natural frequency is discussed further shortly. Equations (19) and (20) then transform back into the time domain to yield

$$\left.\frac{\partial C}{\partial y}\right|_{y=1} = -\Re\{\Psi(\text{Pe}_G)\}[\bar{C} - C_w], \tag{23}$$

$$\left.\frac{\partial T}{\partial y}\right|_{y=1} = -\Re\{\Psi(\text{Pe}_T)\}[\bar{T} - T_w], \tag{24}$$

where the imaginary part of the transfer function, $\Im\{\Psi(\text{Pe})\}$, has necessarily been neglected in order to satisfy Eq. (22). In the above equations, the frequency-independent transfer function is defined as $\Psi(\text{Pe}) \equiv \Psi(1;\text{Pe})$, and the linear perturbations have been written in terms of the original variables.

Comparing the above equations to the approximations (8), it is apparent that the transfer coefficients are given by

$$\beta_C \equiv \Re\{\Psi(\text{Pe}_G)\} \quad \text{and} \quad \beta_T \equiv \Re\{\Psi(\text{Pe}_T)\}. \tag{25}$$

These final two equations close the set of model equations presented in Sec. III A without the need for POD analysis. In Sec. IV, we will test the reduced-order model by comparison to full computations.

In the remainder of this section, we comment on some of the consequences of evaluating the transfer function at a single frequency and neglecting the imaginary part of the transfer function. Figure 6 plots the real part, β, and phase, θ, of the transfer function as the Peclet number is varied over many orders of magnitude. We see in the limit $\text{Pe} \ll 1$, which corresponds to nearly isothermal (and nearly uniform concentration) behavior, that $\beta \to 5$ and $\theta \to 0$. So for this case, the transfer function *is* constant *and* real valued, and the transformations from frequency domain to time domain can be carried out exactly. Hence, for linear perturbations the model equations will become exact as Pe_T and $\text{Pe}_G \to 0$. It is demonstrated in Preston[7] that this property also holds in the more general nonlinear case.

Away from the low Peclet number limit, we choose the isothermal natural frequency at which to evaluate the transfer function in order to avoid a convolution integral on transformation back into the time domain. Obviously during a general bubble motion, there is more than one frequency, so the best we can do is to select the single frequency of the mode that is most affected by the damping effect of the heat and mass transfers, that is, the resonant frequency. When the damping is small, the resonant frequency is close to the natural frequency, which we adopt for simplicity. We also choose to use the isothermal natural frequency, rather than the polytropic natural frequency. This simplification holds for smaller bubbles, while for larger bubbles the polytropic frequency is up to $\gamma^{1/2}$ higher than the isothermal. For air ($\gamma = 1.4$) this is a difference of less than 20%, which is insignificant in comparison to the other approximations already made. An alternative choice of frequency, based on the time scale of forcing, is examined in Preston.[7] He also presents analysis to show that the ringing frequency of bubble collapses and rebounds of moderate amplitudes also scale with the bubble natural frequency, further validating this choice of frequency.

The imaginary part of the transfer function is also neglected after the transformation into the time domain. In the linear analysis, a nonzero imaginary part is related to a phase difference between the gradient and average value, and this phase difference increases with Peclet number. Under these circumstances, the model cannot accurately replicate the complicated behavior of the temperature field that is observed in full computations. However, as detailed in Preston,[7] the POD results in Sec. II C show that this particular detail is not of major importance since the vast majority of the energy is captured in the first POD mode. The POD results are used to further validate the use of the linear analysis in the determination of the transfer coefficients by superposing the values of β_T and β_C determined from POD analysis of full computations on the upper plot of Fig. 6. Each of the data points represents an average of many computations of different forcing amplitude and width at the given Peclet number.

While the data points generally follow the trend predicted by the linear analysis, the value of β derived from the concentration fields at $\text{Pe} = 28.8$ is lower than expected. This is a result of the rather complex concentration fields illustrated in Fig. 2. In particular, at instances (b) and (e) in Figs. 2 and 3, the instantaneous mass-transfer coefficient, β_C, is negative. This impacts the shape of the first POD mode by reducing the slope at the bubble wall, which effectively decreases the value of β obtained from the POD analysis. The impact of the negative instantaneous *heat*-transfer coefficient, β_T, on the value of β obtained from the POD analysis, is not as great since β_T is negative for less time than β_C (as indicated on Fig. 3). The more complex concentration fields are thought to be a result of the mass diffusion being forced by the time-varying concentration at the bubble wall. In contrast, the thermal diffusion is forced by the compression heating term acting (relatively uniformly) over the bubble interior with the wall temperature remaining practically constant. Regardless of the discrepancies for some of the POD results, the data points *generally* follow the trend predicted by linear analysis. This indicates that linear analysis is a good means of determining the transfer coefficients in the absence of POD data.

Finally, an analysis for low Peclet numbers (Preston[7]) shows that the constant-transfer model agrees with the series expansion of the full *nonlinear* equations for C and T to first order in the Peclet numbers.

IV. EVALUATION OF MODELS

In this section, we investigate the accuracy of the constant-transfer model by comparing results directly to full-bubble computations. We note that there are some experimental data with which the models could be compared, but they are not extensive enough to allow a comparison over a wide range of parameter values. Moreover, there are a large number of competing physical effects that determine the ultimate behavior of, for example, bubble radius history. We regard it as more systematic to compare to numerical solutions of the full equations (which, for example, already implicitly assume spherical bubbles), *so that particular modeling assumptions can be tested in isolation*. Aside from the use of constant transfer coefficients (the topic of this paper), other assumptions used in developing this model were tested against the full computations; a full account of those tests is given in Preston.[7] Finally, because we only compare with numerical simulations, the results should be interpreted strictly as necessary conditions for correctness of the resulting model. It is left for future work to evaluate the model in more realistic environments, for example where effects such as liquid compressibility and nonspherical effects are important. We test the model for a variety of forcings, ranging from the Gaussian pulses used in previous sections to harmonic forcing where the frequency and amplitude are varied systematically. In addition, we adapt the constant-transfer model to one that assumes the mass diffusion to be infinitely fast, and we examine pure gas bubbles. This enables the thermal and mass-transfer modeling to be assessed independently.

A. Gas-vapor bubbles

Figures 7 and 8 compare the different models with a full computation for two Gaussian pressure pulses of very different time scales. Note that ν denotes the total effective kinematic viscosity nondimensionalized by ν_L and that κ_{eff} is the effective polytropic index.

While the constant-transfer model slightly overestimates the initial growth and overdamps the rebounds, it is better than the other reduced-order models that show greater departures from the full computation. In particular, the polytropic model significantly underestimates the initial bubble growth, due to $\kappa_{\text{eff}}=1.21$ being determined from linear analysis.[1] In reality, the time scales for the initial bubble growth under the present imposed pressures are far slower than the time scale that is associated with the bubble natural frequency that was used to compute κ_{eff}, so the true behavior is closer to isothermal, $\kappa_{\text{eff}}=1$. Interestingly, though the constant-transfer model also uses the bubble natural frequency to compute transfer coefficients, it is clearly not as sensitive to that value.

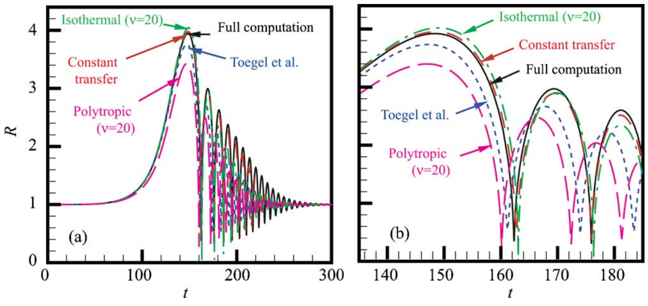

FIG. 7. (Color online) Bubble radius (on two different time scales) computed with full computation and a variety of models for a gas-vapor bubble with $\text{Pe}_T=36.4$ and $\text{Pe}_G=28.8$; constant-transfer model ($\beta_T=6.62, \beta_C=6.21$), model of Toegel *et al.*, isothermal model ($\nu=20$), polytropic model ($\kappa_{\text{eff}}=1.21, \nu=20$). [Parameters same as Fig. 1 (Case E, $A=0.985$).]

The isothermal model makes a better estimate of the slow initial growth than the polytropic model, but the growth is overestimated. This is likely due to the infinitely fast diffusion of vapor, as explained at the end of this section. There are also problems with the isothermal model that are associated with the use of an effective dimensionless liquid viscosity, ν, greater than unity in order to account for damping due to the otherwise neglected diffusive effects. The value $\nu=20$ is chosen to match linear analysis of the full diffusion equations,[1] and works reasonably well for the first bubble rebound in Fig. 7(b). However, it increasingly overdamps the subsequent rebounds. Furthermore, in Fig. 8(b) the same value of effective viscosity results in underattenuated bubble rebounds. This might be corrected by using a higher effective viscosity, but the fact that the appropriate value to use is not known *a priori* is a limitation of that approach.

The model of Toegel *et al.*[6] (and the similar model used by Matula *et al.*[17]) uses fluxes based on estimates of the diffusive penetration lengths. The time scale used in their estimates is $t_R \propto R/|\dot{R}|$, where the overdot denotes a derivative with respect to time. This time scale results in low heat and mass transfer during the final stage of collapse and initial rebound when $\dot{R}\approx 0$. While the duration of this behavior is so short as to not adversely impact the bubble dynamics, the model of Toegel *et al.* has limitations due to the equations not matching the full equations in the limit of low Pe (slow time scales). In this limit, the diffusive penetration length estimated using t_R may approach or exceed the bubble radius. To account for this situation, Toegel *et al.* place a cutoff limit of R/π on the thermal penetration length. This corresponds to implementing a lower limit of π on the transfer coefficient β. However, the analysis for low Peclet numbers included in Preston[7] demonstrates that the correct lower limit is 5 (as is also indicated empirically in Fig. 6).

The impact of the incorrect cutoff is demonstrated in both Figs. 7 and 8, where the model of Toegel *et al.* under-

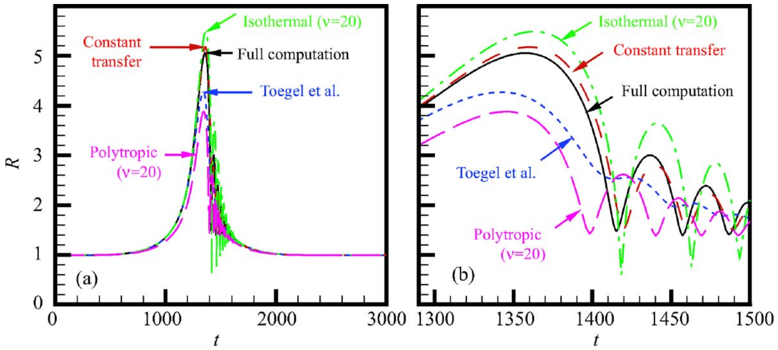

FIG. 8. (Color online) Bubble radius (on two different time scales) computed with full computation and a variety of models for a gas-vapor bubble with $\mathrm{Pe}_T=36.4$ and $\mathrm{Pe}_G=28.8$; constant-transfer model ($\beta_T=6.62,\beta_C=6.21$), model of Toegel *et al.*, isothermal model ($\nu=20$), polytropic model ($\kappa_{\mathrm{eff}}=1.21,\nu=20$). The time scale of the pulse is an order of magnitude larger than that in Fig. 7. [Parameters same as Fig. 7, except $A=0.97$ and $t_w=435$ (Case F, $A=0.97$).]

estimates the initial growth. This is more evident in the latter figure, for which the forcing is ten times slower. We would like to clarify here that we only implemented the *flux* models of Toegel *et al.* in our comparisons. Other aspects of their model, such as the van der Waals equation of state and liquid compressibility, were not implemented. Implementing only the heat and mass fluxes of the model of Toegel *et al.*, while keeping other assumptions consistent with our model and our full bubble computation, enables the modeling of the heat and mass transfer to be studied in isolation.

A systematic evaluation of the relative errors in $R_{\max}$, R_{rebound}, $R_{\min}$, $T_{\max}$, $p_{\max}$, and $\bar{C}_{\min}$ (as defined in Sec. II A) was also undertaken for a range of the parameters t_w, A, Pe_T, and Pe_G. The results of this analysis are presented in Preston[7] and are only summarized here. The errors in all the variables are consistently lower for the constant-transfer model than for other reduced-order models. In particular, the constant-transfer model yields estimates of $R_{\max}$ within a few percent of the full computation. For moderate bubble growths, the important variable, R_{rebound}, is also within a few percent of the full computation, while for some larger bubble growths the errors are as high as 30%. The errors in $R_{\min}$ are typically within 20–30%, except for one data point where the error is as high as 80%. In the context of the small minimum radii, such large relative errors do not have significant consequences. In any case, the estimates of $R_{\min}$ of the constant-transfer model are more accurate than those of the other models. The constant-transfer model yields estimates for $T_{\max}$ within about 20% of the full computations. Estimates of $p_{\max}$ and $\bar{C}_{\min}$ from the constant-transfer model are only accurate to within an order of magnitude, but these are more accurate than those from the other reduced-order models.

The model comparisons were only made for situations in which $R_{\max}$ is less than about 10. While the model equations can be solved for greater bubble growths, the full computation is impeded by the large spatial gradients in C and T that exist near the bubble wall during violent collapse. To resolve these large gradients, additional spectral modes are required that, due to stability constraints of the explicit time-marching scheme, result in the time step being reduced to near the limit of machine accuracy. This limitation of the full computation prevents full validation of the models at higher values of $R_{\max}$. Similarly large spatial gradients also occur at higher values of Peclet number, which prevents full validation of the model in these situations. Future full-bubble computations using an implicit time-marching scheme may be able to overcome these restrictions.

Finally, we modify the constant-transfer model to one that assumes mass diffusion to be infinitely fast, while retaining the heat diffusion model. We recognize that this is a purely hypothetical situation, since the mass and thermal diffusivities are generally of the same order. This situation is examined in order to illustrate the importance of the mass diffusion modeling. The modification is achieved by redefining the pressure, p, in Eqs. (5) and (6) to be the partial pressure of noncondensible gas, p_A. The constant vapor pressure, p_{vsat}, is then added to Eq. (5) and the $\dot{m}_V$ term is removed from Eq. (6) to yield

$$\mathrm{Eu}[p_A+p_{\text{vsat}}-p_\infty(t)]=R\frac{d^2R}{dt^2}+\frac{3}{2}\left(\frac{dR}{dt}\right)^2+\frac{4}{\mathrm{Re}}\frac{1}{R}\frac{dR}{dt}+\frac{2}{\mathrm{We}R}, \tag{26}$$

$$\frac{dp_A}{dt}=\frac{-3\gamma}{R}\left(p_A\frac{dR}{dt}-\frac{1}{\mathrm{Pe}_T}\frac{1}{R}k_w\left.\frac{\partial T}{\partial y}\right|_{y=1}\right). \tag{27}$$

Equations (7) and (12) are then replaced by

$$m_V=\frac{m_{A0}}{\xi}, \tag{28}$$

where ξ is given by Eq. (10). The above equation is derived by noting that $\bar{C}=C_w$ for infinitely fast mass diffusion, which enables Eq. (9) and approximation (13) (that is now exact due to the uniform concentration distribution) to be combined.

The bubble radius determined by the full computation is compared to the constant-transfer model for both finite and infinitely fast mass diffusion in Fig. 9(a). It is apparent that infinitely fast mass diffusion results in overestimation of the initial bubble growth and subsequent rebounds, and underestimation of the bubble minimum radii.

Plots of the average and wall vapor concentrations in Fig. 9(b) show a higher average vapor concentration for the model with fast mass diffusion, which indicates that the overestimation of the bubble growth is due to too much evaporation into the bubble. Similarly, the underestimation of the bubble minimum radii is caused by too much vapor

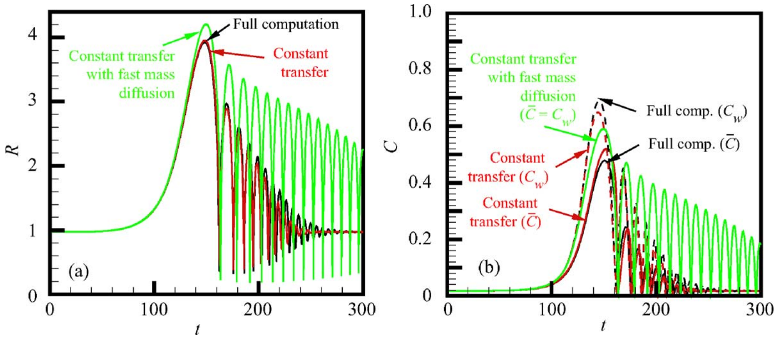

FIG. 9. (Color online) (a) Bubble radii and (b) concentrations computed with the full computation, the constant-transfer model with finite rate mass-diffusion modeling, and the constant-transfer model with infinitely fast mass diffusion. The bubble consists of gas and vapor with $\mathrm{Pe}_T=36.4$ and $\mathrm{Pe}_G=28.8$. [Parameters same as Fig. 1 (Case E, $A=0.985$)].

condensing out of the bubble during collapse. Although it is not clear on the scale of Fig. 9(b), the average vapor concentration during collapse obtained from the model with fast mass diffusion is an order of magnitude lower than it is for the full computation and the constant-transfer model with finite rate diffusion. It is obvious that the vapor-trapping effect identified by Storey and Szeri[10] is important in this particular circumstance, and the mass-diffusion modeling in the constant-transfer model is able to capture this behavior. This may have important consequences in sonochemistry, where the amount of vapor trapped in the bubble during collapse would impact the chemical reactions. In the present application to bubble dynamics, the modeling of mass diffusion is important during the collapse stage to avoid the unrealistically small minimum radii observed in Fig. 9(a) for the model with fast mass diffusion.

Thus, in order to accurately model the bubble dynamics, it is necessary to account for finite rate mass diffusion of vapor during *both* expansion and collapse. The constant-transfer model with finite rate diffusion is able to predict the average and wall vapor concentrations reasonably well, resulting in good predictions of the bubble radius.

B. Gas bubbles

We now shift attention to pure gas bubbles in order to evaluate the heat-transfer component of the constant-transfer model. Figure 10 compares computed bubble radii of different models to the full computation for two gas bubbles with $\mathrm{Pe}_T=4.61$ and 34.8. For the lower value of Pe_T [Fig. 10(a)], the behavior is close to the isothermal limit, and, as anticipated, the constant-transfer model is essentially identical to the full computation. In addition, the nearly isothermal model of Prosperetti[18] agrees almost exactly with the full computation, since this is within the limit for which the model is valid. The model of Storey and Szeri[19] underestimates the attenuation because there is no thermal damping in their model. The polytropic model with effective viscosity (chosen to match linear analysis) underestimates the initial growth, probably due to too much viscous damping.

For the bubble with larger Pe_T, the behavior departs from the isothermal limit. Figure 10(b) shows that the constant-transfer model accurately captures the initial bubble growth and the attenuation of the bubble rebounds. The absence of thermal damping in the switching model of Storey results in the slow decay of the rebounds. By contrast, the nearly isothermal model of Prosperetti overpredicts the attenuation of the bubble rebounds. The polytropic model also behaves poorly since, as explained in Sec. IV A, the use of a polytropic index of $\kappa_{\mathrm{eff}}=1.21$ prevents the correct prediction of the initial expansion, which is relatively slow and therefore nearer the isothermal limit. Again, it seems that the constant-transfer model can correctly capture the nearly isothermal expansion even though we use a value of β_T that has been chosen to match behavior away from this limit.

C. Harmonic forcing

The constant-transfer model is intended for application to bubbles exposed to pressure excursions that may arise in complicated bubbly flows. While the previously used Gaussian pressure pulses provide a quick means of testing reduced-order models for a variety of forcings, it is also valuable to test them with harmonic forcings over a range of frequencies and amplitudes. In this section, we compare the constant-transfer model with the often used polytropic model (using the effective values of polytropic index, κ_{eff}, and effective

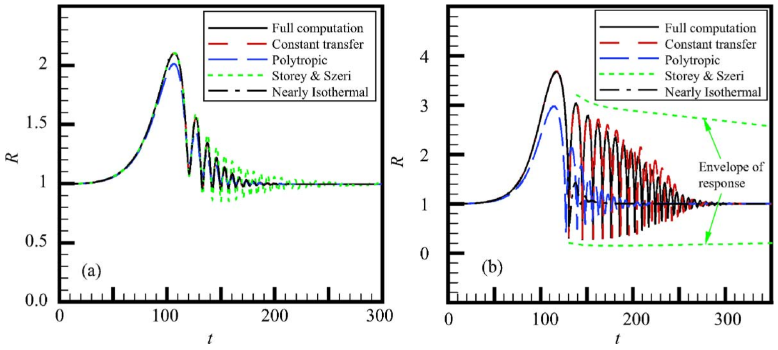

FIG. 10. (Color online) Computed radii for two gas bubbles subject to a Gaussian decrease in far-field pressure. The curves show comparisons to the full computation of the constant-transfer model, the polytropic model with effective damping, the switching model of Storey and Szeri, and the nearly isothermal model of Prosperetti. (a) $\mathrm{Pe}_T=4.61$ (Case I, $\beta_T=5.05$, $\nu=2.6$, $\kappa_{\mathrm{eff}}=1.03$); (b) $\mathrm{Pe}_T=34.8$ (Case J, $\beta_T=6.54$, $\nu=20$, $\kappa_{\mathrm{eff}}=1.21$).

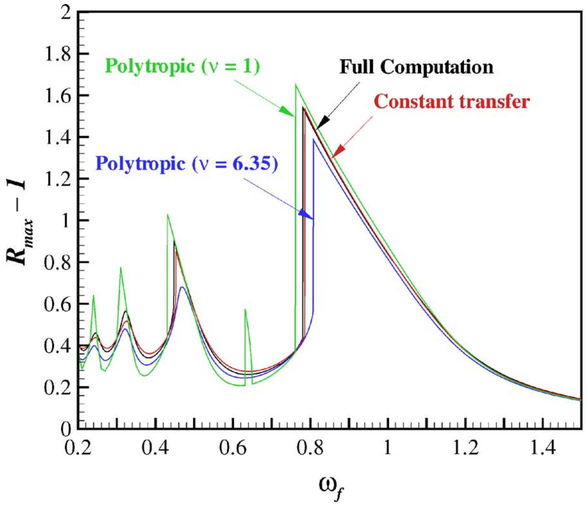

FIG. 11. (Color online) Frequency-response curves for the forced oscillations of a gas bubble (Pe_T=9.26, Case K) for a dimensionless pressure amplitude A=0.6. The results of the constant-transfer model (β_T=5.18) are compared to the full computation and to the polytropic model with and without effective damping (ν=6.35 and 1, κ_{eff}=1.079).

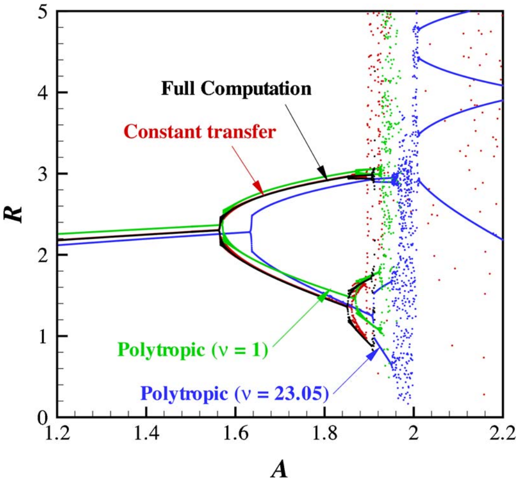

FIG. 12. (Color online) Bifurcation diagram of the bubble radius sampled at every period of the forcing pressure for a gas bubble (Pe_T=42.9, Case L) driven with forcing frequency ω_f=0.8 and a slowly increasing pressure amplitude, A. The results of the constant-transfer model (β_T=6.96) are compared to the full computation and to the polytropic model with and without effective damping (ν=23.05 and 1, κ_{eff}=1.230).

liquid viscosity, ν, obtained to match linear theory[1]) and the full computation of the complete conservation equations. We use the harmonic forcing pressure

$$p_\infty(t) = p_{\infty 0}(1 + A \sin \omega_f t), \tag{29}$$

where A is the amplitude and ω_f is nondimensionalized by the linear natural bubble frequency. In this context, it is clear that the best frequency for computing the appropriate value of β_T in the constant-transfer model would be ω_f. However, in order to provide an unbiased test of the model that can be extrapolated to general forcing, we compute β_T using the bubble natural frequency by setting ω=1 in Eq. (21), regardless of the actual forcing frequency. To be consistent, we also use ω_f=1 when computing the value of effective polytropic index and damping in the polytropic model.

Figure 11 presents the response of a gas bubble with Pe_T=9.26 and amplitude A=0.6 over a range of frequencies and shows the maximum value of bubble radius attained during a steady oscillation. The results are obtained by integrating the equations forward in time until a steady-state cycle is achieved. It should be noted that around each of the harmonic peaks there actually exist two different stable steady-state solutions.[20,21] The solution that is found depends on the initial conditions. The present calculations are started with a bubble in static equilibrium (R=1 and $\dot{R}$=0) and converge to only one of these solutions. If other initial conditions were chosen, the hysteresis behavior typical of many nonlinear systems would become evident.

The constant-transfer model shows excellent agreement with the full computation over all frequencies, even though the model uses ω_f=1. In contrast, as first identified by Prosperetti *et al.*,[1] neither of the polytropic models is able to predict the location and magnitude of the harmonic peaks. Indeed, the behavior of the polytropic model depends strongly on the value of effective damping that is used. This poor feature of the polytropic model is further emphasized by the existence of a peak at $\omega_f \approx 0.63$ when ν=1. This spurious peak is caused by a 3/2 ultraharmonic mode that results in period doubling of the bubble response. The existence of this peak, and additional ultraharmonic peaks at higher forcing amplitudes,[21] can give rise to gross errors in the response of the polytropic model if the effective damping is not high enough.

The accuracy of the constant-transfer model for a larger Peclet number (Pe_T=42.9) and various forcing amplitudes is presented in Fig. 12. This shows a bifurcation diagram of the computed bubble radius sampled at every period of forcing for a gas bubble driven at a forcing frequency ω_f=0.8 with an incrementally increasing pressure amplitude. Once steady state was reached at A=1.2, the pressure was increased at a rate of 10^{-3} per cycle up to A=1.5 and then at a rate of 10^{-4} per cycle. The results of the constant-transfer model (β_T=6.96) are compared to the full computation and to the polytropic model with and without effective damping (ν=23.05 and 1).

The curve for the polytropic model with effective damping (ν=23.05) is shifted significantly to the right and below the full computation. Interestingly, the polytropic model without effective damping (ν=1) yields results that agree more closely with the full computation, although the radius is slightly higher due to the lack of thermal damping. It appears that the addition of effective damping to the polytropic model substantially delays the onset of the bifurcations and overdamps the bubble response. In addition, at higher forcing amplitude ($A \gtrsim 2$), the polytropic model with effective damping returns from the chaotic oscillations to the subharmonic oscillations. The use of this model in certain regimes could result in gross errors in predicted bubble response.

By contrast, the constant-transfer model shows good agreement with the full computation over a range of forcing amplitudes. Agreement is excellent through the first subharmonic bifurcation at $A \approx 1.56$. The agreement at the second harmonic bifurcation is not as good, with the full computation giving the bifurcation at $A \approx 1.85$ while the constant-transfer model bifurcated at $A \approx 1.86$. Chaotic oscillations set in at $A \approx 1.91$ for the full computation and at $A \approx 1.90$ for the constant-transfer model. The exact form of these chaotic oscillations was found to depend strongly on numerical tolerances in the integration as well as the rate at which the amplitude is increased.

V. CONCLUSIONS

A new *constant-transfer* model of the heat- and mass-transfer effects on bubble dynamics has been developed. The constant-transfer model relates the temperature and concentration gradients at the bubble wall to the volume-averaged bubble temperature and concentration through the use of constant heat- and mass-transfer coefficients. The model was motivated by examining detailed simulations of the full governing equations for spherical bubbles, and by systematic analysis of the results using proper orthogonal decomposition (POD). The values of the transfer coefficients could be determined directly from the first POD mode, and were demonstrated to depend on the Peclet number. Linear analysis of the diffusion equations was also presented as a means for determining the transfer coefficients, without the need for POD results. The model equations become exact as the Peclet numbers tend to zero. The constant-transfer model requires at most three ordinary differential equations to accurately capture diffusive effects, enabling it to be readily implemented into existing and future algorithms for complicated bubbly flows.

The results show that the use of constant heat- and mass-transfer coefficients is reasonable over a large parameter space. The model was found to capture the bubble dynamics with good accuracy. In particular, the amplitudes of bubble growth and rebound were within a few percent of the full computations, while the maximum internal temperature on collapse was within about 20%. The maximum pressures and minimum vapor concentrations in the bubble upon collapse are less accurately predicted, with model values only within an order of magnitude of those from the full computation.

As expected, the model works extremely well for Peclet numbers below about 10. At higher Peclet numbers, the model equations neglect the phase difference between the gradient at the bubble wall and the average bubble value. However, this does not have too serious an effect on the results for the parameter space considered in this paper. It remains for the model to be tested at even larger Peclet numbers and bubble growths than those considered in this paper. However, this is limited by the difficulty with the full computation, which is impeded by the very large spatial gradients in temperature and concentration near the bubble wall.

ACKNOWLEDGMENTS

The authors are grateful for the support from the NSF under Grant No. CTS 9979258 and the NIH under Grant No. PO1 DK43881.

[1] A. Prosperetti, L. A. Crum, and K. W. Commander, "Nonlinear bubble dynamics," J. Acoust. Soc. Am. **83**, 502 (1988).

[2] M. Watanabe and A. Prosperetti, "Shock waves in dilute bubbly liquids," J. Fluid Mech. **274**, 349 (1994).

[3] Y. Matsumoto and F. Takemura, "Influence of internal phenomena on gas bubble motion," JSME Int. J., Ser. B **37**, 288 (1994).

[4] M. Kameda and Y. Matsumoto, "Shock waves in a liquid containing small gas bubbles," Phys. Fluids **8**, 322 (1996).

[5] A. Prosperetti and A. Lezzi, "Bubble dynamics in a compressible liquid. Part 1: First-order theory," J. Fluid Mech. **168**, 457 (1986).

[6] R. Toegel, B. Gompf, R. Pecha, and D. Lohse, "Does water vapor prevent upscaling sonoluminescence?," Phys. Rev. Lett. **85**, 3165 (October 2000).

[7] A. T. Preston, "Modeling heat and mass transfer in bubbly cavitating flows and shock waves in cavitating nozzles," Ph.D. thesis, California Institute of Technology (2004).

[8] Y. Hao and A. Prosperetti, "The dynamics of vapor bubbles in acoustic pressure fields," Phys. Fluids **11**, 2008 (1999).

[9] A. T. Preston, T. Colonius, and C. E. Brennen, "A numerical investigation of unsteady bubbly cavitating nozzle flows," Phys. Fluids **14**, 300 (2002).

[10] B. D. Storey and A. J. Szeri, "Water vapour, sonoluminescence and sonochemistry," Proc. R. Soc. London, Ser. A **456**, 1685 (2000).

[11] R. I. Nigmatulin, N. S. Khabeev, and F. B. Nagiev, "Dynamics, heat and mass transfer of vapour-gas bubbles in a liquid," Int. J. Heat Mass Transfer **24**, 1033 (1981).

[12] C. E. Brennen, *Cavitation and Bubble Dynamics* (Oxford University Press, New York, 1995).

[13] V. Q. Vuong and A. J. Szeri, "Sonoluminescence and diffusive transport," Phys. Fluids **8**, 2354 (1996).

[14] W. C. Moss, D. A. Young, J. A. Harte, J. L. Levatin, B. F. Rozsnyai, G. B. Zimmerman, and I. H. Zimmerman, "Computed optical emissions from a sonoluminescing bubble," Phys. Rev. E **59**, 2986 (1999).

[15] C. W. Rowley, "Modeling, simulation, and control of cavity flow oscillations," Ph.D. thesis, California Institute of Technology (2002).

[16] L. Sirovich, "Turbulence and the dynamics of coherent structures, parts I-III," Q. Appl. Math. **45**, 561 (1987).

[17] T. J. Matula, P. R. Hilmo, B. D. Storey, and A. J. Szeri, "Radial response of individual bubbles subjected to shock wave lithotripsy pulses *in vitro*," Phys. Fluids **14**, 913 (March 2002).

[18] A. Prosperetti, "The thermal behaviour of oscillating gas bubbles," J. Fluid Mech. **222**, 587 (1991).

[19] B. D. Storey and A. J. Szeri, "A reduced model of cavitation physics for use in sonochemistry," Proc. R. Soc. London, Ser. A **457**, 1685 (2001).

[20] A. Prosperetti, "Nonlinear oscillations of gas bubbles in liquids: Steady-state solutions," J. Acoust. Soc. Am. **56**, 878 (1974).

[21] W. Lauterborn, "Numerical investigation of nonlinear oscillations of gas bubbles in liquids," J. Acoust. Soc. Am. **59**, 283 (1976).